Numerical modeling of guided wave interaction with non-axisymmetric cracks in elastic cylinders

Farouk Benmeddour, Fabien Treyssede, Laurent Laguerre

Numerical modeling of guided wave interaction with non-axisymmetric cracks in elastic cylinders

Farouk BENMEDDOUR, Fabien TREYSSÈDE, Laurent LAGUERRE

University of Nantes, Laboratoire Central des Ponts et Chaussés, Route de Bouaye, BP 4129, 44341 Bouguenais, France.

Abstract

A three dimensional (3D) hybrid method combining the classical finite element (FE) method with the semi-analytical finite element (SAFE) technique is developed. This hybrid method is employed to study the interaction of guided waves with non-axisymmetric damages in cylinders. The near field surrounding the damage is analysed with the 3D FE method. The solution is expanded into sums of guided modes on both inlet and outlet cross-sections. Such eigenmode expansions enable separation into ingoing and outgoing waves, i.e., incident, reflected and transmitted waves. Using the SAFE method, elastic guided modes are then computed at the aforementioned cross-sections thus reducing the analysis to two dimensions (2D). The amplitudes of the incident modes are imposed, whereas those of the scattered modes are determined by solving the global system of the 3D hybrid FE-SAFE model. In this paper, a formula is proposed for the calculation of eigenforces and modal power flows from eigendisplacements and SAFE matrices. This has the advantage of simplifying the post-process of load eigenvectors in hybrid FE-SAFE methods. Results obtained for a vertical free-end cylinder are in good agreement with those published in the literature. Moreover, first

results of the interaction of the fundamental compressional, flexural and torsional Pochhammer-Chree modes with non-axisymmetric vertical cracks are obtained and discussed. Then, the interactions of the fundamental compressional mode with oblique free-ends and cracks are briefly addressed. The power balance is shown to be satisfied with a good accuracy.
Key words: Guided waves, Cylinders, Cracks, 3D Hybrid FE-SAFE.

1. INTRODUCTION

Non-destructive testing (NDT) techniques using guided ultrasonic waves constitute viable inspection means for tubes, pipes and plates owing to their potential to carry out energy over long distances and their sensitivity to internal damages. Nevertheless, the interaction of such waves with damages is complex since elastic guided waves are multi-modal and dispersive. This highlights the essential role of modeling techniques in providing a better understanding of and a deeper insight into the nature of phenomena arising from scattering problems.

Various analytical approaches have been proposed in the literature. For instance, one can cite quasi-static approximations based on the S-parameter formalism for plates (Auld, 1973) and tubes (Ditri, 1994), and modal decomposition methods recently developed for plates (Le Clézio et al., 2002; Castaings et al., 2002; Demma et al., 2003; Shkerdin and Glorieux, 2004, 2005). Such methods are fast from a computational point of view but generally limited to simple geometries with horizontal or vertical discontinuities.

Fully numerical approaches based on transient finite element (FE) analyses have been conducted for plates (Alleyne and Cawley, 1992; Lowe and Dili-

gent, 2002; Benmeddour et al., 2008b,a) and pipes (Lowe et al., 1998; Demma et al., 2004; Ma et al., 2006). The main advantage of these approaches is that complex-shaped waveguides or damages can be handled with standard FE codes. However, transient FE models are time consuming, which often limits their practical use to two-dimensional problems and short propagation distances. Besides, a modal post-processing step in the frequency domain must be performed, which requires an *a priori* knowledge of guided modes. Recently, Gunawan and Hirose (2004) have developed a mode-exciting method to analyse the interaction of Lamb waves with defects. The originality of their work is in the analysis of a finite plate model using a standard FE or boundary element (BE) method software with a time-harmonic regime. However, in addition to the *a priori* knowledge of guided modes, their analysis requires a great number of computations at high frequencies. Moreau et al. (2006) and Predoi et al. (2008) have used an existing FE software with absorbing regions at the edge of plates. Harmonic FE solutions have been post-processed with the help of a general orthogonality relation.

Hybrid approaches, combining a FE method and the so-called normal mode expansion technique have been developed for studying wave scattering by damages in plates (Karunasena et al., 1991, 1994; Al-Nassar et al., 1991; Mal and Chang, 2000). They consist in performing a modal decomposition both at the inlet and outlet of a waveguide FE model. It can then be limited to a small region surrounding the damage. The modal decomposition is performed by virtue of analytical solutions for the guided modes of the considered structure. The scattered solution is computed for each frequency and directly yields the coefficients of scattered modes without any

post-processing. The same procedure based on a BE method has also been applied by Zhao and Rose (2003).

In the literature, analytical solutions for guided modes, limited to simple cross-section geometries, have been replaced in several occasions by the semi-analytical finite element (SAFE) technique (see e.g. Lagasse (1973); Gavrić (1995); Hladky-Hennion (1996); Hladky-Hennion et al. (1997); Damljanović and Weaver (2004); Hayashi et al. (2003, 2006)). This has given rise to the so-called hybrid FE-SAFE and BE-SAFE methods capable of handling arbitrary cross-sections with complex-shaped damages. The former has been successfully applied to two-dimensional geometries such as plates (Karunasena et al., 1995; Datta et al., 1999) and cylinders (Rattanawangchroen et al., 1997; Zhuang et al., 1997), and so has been the latter for plates (Galán and Abascal, 2003, 2005). It is noteworthy that the periodic FE method can be seen as an alternative for the SAFE method when dealing with arbitrary cross-sections, as proposed by Zhou et al. (2009) for the study of thin pipes with non-axisymmetric damages. In a mathematical framework, a Dirichlet-to-Neumann approach has also recently been proposed for isotropic plates (Baronian et al., 2010) based on a mixed formulation and biorthogonality relation.

The aim of this work is to study the interaction of guided waves with non-axisymmetric cracks in infinite circular cylinders. Such a study requires a three dimensional (3D) formulation. To this end, a general 3D hybrid FE-SAFE procedure is developed in Sec. 2. The 3D variational formulation of elastodynamics is first recalled. A modal expansion is applied at the cross-section boundaries of the waveguide, which enables the separation between

ingoing and outgoing modes. Eigenmodes are computed using the SAFE technique. A formula is proposed for the direct calculation of eigenforces from SAFE matrices. For hybrid FE-SAFE methods, this may greatly simplify the post-process of consistent load eigenvectors, usually performed from displacement derivatives. In the same way, expressions for power reflection and transmission coefficients are also presented. This paves the way for the implementation of hybrid FE-SAFE methods inside standard FE softwares.

Section 3 deals with the interaction of the fundamental Pochhammer-Chree modes with a free-end and non-axisymmetric vertical cracks inside circular isotropic cylinders. For the free-end cylinder, the obtained results are in good agreement with those already published in the literature. For non-axisymmetric vertical cracks, the results of their interaction with the fundamental guided modes are obtained and discussed. It should be noted that some of the analytical approaches mentioned earlier could also be used for this kind of discontinuities. However, to the authors' knowledge, vertical cracks inside cylinders have surprisingly not received a great attention in the literature.

Finally, the case of oblique discontinuities is briefly studied in Sec. 4 where different inclination angles are analysed. Results are compared with those obtained for vertical discontinuities.

2. Hybrid FE-SAFE method

2.1. General description of the problem

Figure 1 depicts a damage located inside an arbitrary volume V. This volume is connected to two semi-infinite waveguides of arbitrary cross-sections.

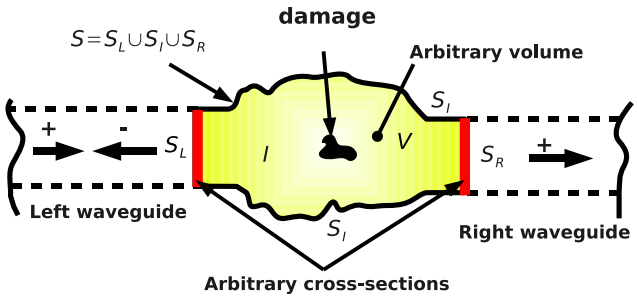

Figure 1: Description of the problem in the case of a damaged volume located between two semi-infinite waveguides (2D representation).

These waveguides are situated on the left (L) and right (R) of the interior region (I) of the volume V. Each cross-section has the same uniform geometry along the propagation direction. Incident waves are launched from the left waveguide in the positive direction (+). Then, reflected waves from the damage travel in the negative direction (−). Transmitted waves in the right waveguide propagate in the positive direction. The interior region is connected to the left and right waveguides through boundaries denoted S_L and S_R, respectively. The whole volume V is bounded by S_L and S_R and by a traction free boundary, denoted S_I.

2.2. Finite element formulation for the interior region

For the volume V, a standard FE method with a time harmonic regime is used. The application of virtual works to the equation of motion governing elastodynamics gives, after dropping the time dependence $e^{-j\omega t}$, the following variational formulation:

$$\int_V \delta\boldsymbol{\epsilon}^T \boldsymbol{\sigma} dV - \omega^2 \int_V \rho \delta \mathbf{u}^T \mathbf{u} dV - \int_S \delta \mathbf{u}^T \mathbf{t} dS = 0, \tag{1}$$

where $S = S_L \cup S_I \cup S_R$ is the boundary surrounding the volume V, $\delta(\cdot)$ denotes virtual fields, ω is the angular frequency and ρ is the material density. $\mathbf{u} = [u_x \ u_y \ u_z]^T$ is the vector of time harmonic displacements, where x, y and z are cartesian coordinates and the superscript T denotes transpose, $\boldsymbol{\epsilon} = [\epsilon_{xx} \ \epsilon_{yy} \ \epsilon_{zz} \ 2\epsilon_{xy} \ 2\epsilon_{xz} \ 2\epsilon_{yz}]^T$ is the strain vector and $\boldsymbol{\sigma} = [\sigma_{xx} \ \sigma_{yy} \ \sigma_{zz} \ \sigma_{xy} \ \sigma_{xz} \ \sigma_{yz}]^T$ is the stress vector. The stress-strain relationship is given by $\boldsymbol{\sigma} = \mathbf{C}\boldsymbol{\epsilon}$, $\mathbf{C}$ is the elastic coefficient matrix. $\mathbf{t} = [t_x \ t_y \ t_z]^T$ represents the external traction defined from: $t_i = \sigma_{ij} n_j \ (i, j = x, y, z)$, where $\mathbf{n} = [n_x \ n_y \ n_z]^T$ is the outward normal to the surface S.

The FE discretisation of the volume V leads to an approximation of the displacement field $\mathbf{u}$ based on the use of interpolating functions. For a given element e, the approximation of displacement is $\mathbf{u} = \mathbf{N}^e \mathbf{U}^e$, where $\mathbf{N}^e$ is the matrix of nodal interpolating polynomials and $\mathbf{U}^e$ is the vector of nodal displacements of the element. Assembling elementary matrices into global ones, Eq. (1) finally yields:

$$\delta \mathbf{U}^T \left(\mathbf{K} - \omega^2 \mathbf{M} \right) \mathbf{U} - \delta \mathbf{U}^T \mathbf{f} = 0, \tag{2}$$

where $\mathbf{U}$ is the vector of degrees of freedom (dofs) of displacement, $\mathbf{K}$ and $\mathbf{M}$ are the global stiffness and mass matrices, respectively, and $\mathbf{f}$ represents a vector of external time harmonic forces.

In this study, interior forces are not considered. The above discretised

variational formulation can be partitioned as follows:

$$\left\{\begin{array}{c}\delta\mathbf{U}_L\\ \delta\mathbf{U}_I\\ \delta\mathbf{U}_R\end{array}\right\}^T \left[\begin{array}{ccc}\mathbf{D}_{LL} & \mathbf{D}_{LI} & \mathbf{D}_{LR}\\ \mathbf{D}_{IL} & \mathbf{D}_{II} & \mathbf{D}_{IR}\\ \mathbf{D}_{RL} & \mathbf{D}_{RI} & \mathbf{D}_{RR}\end{array}\right] \left\{\begin{array}{c}\mathbf{U}_L\\ \mathbf{U}_I\\ \mathbf{U}_R\end{array}\right\} - \left\{\begin{array}{c}\delta\mathbf{U}_L\\ \delta\mathbf{U}_I\\ \delta\mathbf{U}_R\end{array}\right\}^T \left\{\begin{array}{c}\mathbf{f}_L\\ \mathbf{0}\\ \mathbf{f}_R\end{array}\right\} = 0, \tag{3}$$

where $\mathbf{U}_L$, $\mathbf{U}_I$ and $\mathbf{U}_R$ respectively denote the left, interior and right displacement dofs. $\mathbf{D}_{ij} = \mathbf{K}_{ij} - \omega^2\mathbf{M}_{ij}$ $(i, j = L, I, R)$ are the associated partitions.

2.3. Mode expansions on waveguide cross-sections

On S_L and S_R, displacements and forces are expanded into sums of modes. On S_L, the sum is decomposed into ingoing $(+)$ and outgoing $(-)$ modes. On S_R, only the outgoing $(+)$ modes are taken into account which enforces the coefficients of ingoing $(-)$ modes to zero giving rise to a transparent boundary condition. For propagating modes, the traveling direction is determined from the sign of the energy velocity, whereas for non-propagating modes it is determined from the sign of the imaginary part of the wave number.

Displacements and forces on the left and right sections are then given by:

$$\begin{aligned}\mathbf{U}_L &= \textstyle\sum_{n=1}^{N_L^+} \alpha_{Ln}^+ \mathbf{U}_{Ln}^+ + \sum_{n=1}^{N_L^-} \alpha_{Ln}^- \mathbf{U}_{Ln}^- \ ,\\ \mathbf{f}_L &= \textstyle\sum_{n=1}^{N_L^+} \alpha_{Ln}^+ \mathbf{f}_{Ln}^+ + \sum_{n=1}^{N_L^-} \alpha_{Ln}^- \mathbf{f}_{Ln}^- \ ,\end{aligned} \tag{4}$$

and:

$$\begin{aligned}\mathbf{U}_R &= \textstyle\sum_{n=1}^{N_R^+} \alpha_{Rn}^+ \mathbf{U}_{Rn}^+ \ ,\\ \mathbf{f}_R &= \textstyle\sum_{n=1}^{N_R^+} \alpha_{Rn}^+ \mathbf{f}_{Rn}^+ \ ,\end{aligned} \tag{5}$$

where n denotes the mode number, $N_L^{\pm}$ and N_R^{+} are the number of modes considered in the expansions. $\alpha_{Ln}^{\pm}$ $(n = 1, ..., N_L^{\pm})$ and α_{Rn}^{+} $(n = 1, ..., N_R^{+})$ are the left and right displacement modal amplitudes, respectively. From a theoretical point of view, $N_L^{\pm}$ and N_R^{+} should tend to infinity. However, in practice, series are truncated by retaining the less attenuated modes. All the propagating and only some of the non-propagating modes are taken into account. The choice of the number of these non-propagating modes is based on their attenuations, which are related to the imaginary part of the wavenumber.

Eqs. (4) and (5) can be transformed into products of matrices. For the left section, coefficients of positive-going modes are imposed so that $\delta\alpha_{Ln}^{+} = 0$. Displacements, forces and virtual displacements can then be expressed as:

$$\begin{aligned} &\mathbf{U}_L = \mathbf{B}_L^{+}\boldsymbol{\alpha}_L^{+} + \mathbf{B}_L^{-}\boldsymbol{\alpha}_L^{-} \,, \quad && \mathbf{U}_R = \mathbf{B}_R^{+}\boldsymbol{\alpha}_R^{+} \,, \\ &\mathbf{f}_L = \mathbf{T}_L^{+}\boldsymbol{\alpha}_L^{+} + \mathbf{T}_L^{-}\boldsymbol{\alpha}_L^{-} \,, && \mathbf{f}_R = \mathbf{T}_R^{+}\boldsymbol{\alpha}_R^{+} \,, \\ &\delta\mathbf{U}_L = \delta\boldsymbol{\alpha}_L^{-T}\mathbf{B}_L^{-T} \,, && \delta\mathbf{U}_R = \delta\boldsymbol{\alpha}_R^{+T}\mathbf{B}_R^{+T} \,, \end{aligned} \tag{6}$$

with the following notations:

$$\begin{aligned} \boldsymbol{\alpha}_L^{\pm} &= \left[\alpha_{L1}^{\pm}\ \alpha_{L2}^{\pm}\ ...\ \alpha_{LN_L^{\pm}}^{\pm}\right]^T , \\ \mathbf{B}_L^{\pm} &= \left[\mathbf{U}_{L1}^{\pm}\ \mathbf{U}_{L2}^{\pm}\ ...\ \mathbf{U}_{LN_L^{\pm}}^{\pm}\right] , \\ \mathbf{T}_L^{\pm} &= \left[\mathbf{f}_{L1}^{\pm}\ \mathbf{f}_{L2}^{\pm}\ ...\ \mathbf{f}_{LN_L^{\pm}}^{\pm}\right] , \end{aligned} \tag{7}$$

$\boldsymbol{\alpha}_L^{\pm}$ denotes column vectors of the amplitudes of positive and negative going modes of the left section. $\mathbf{B}_L^{\pm}$ defines displacement modal bases. $\mathbf{T}_L^{\pm}$ denote modal bases of forces $\mathbf{f}_{Ln}^{\pm}$. $\mathbf{B}_R^{+}$, $\mathbf{T}_R^{+}$ and $\boldsymbol{\alpha}_R^{+}$ are defined in the same way by replacing the subscripts L with R.

With the help of Eqs. (6), $\delta\mathbf{U}$ can be rewritten as:

$$\langle \delta\mathbf{U}_L \; \delta\mathbf{U}_I \; \delta\mathbf{U}_R \rangle = \left\langle \delta\boldsymbol{\alpha}_L^- \;\; \delta\mathbf{U}_I \;\; \delta\boldsymbol{\alpha}_R^+ \right\rangle \begin{bmatrix} \mathbf{B}_L^{-T} & \mathbf{0} & \mathbf{0} \\ \mathbf{0} & \mathbf{I} & \mathbf{0} \\ \mathbf{0} & \mathbf{0} & \mathbf{B}_R^{+T} \end{bmatrix}, \tag{8}$$

where $\mathbf{I}$ is the identity matrix.

For any trial field $\delta\boldsymbol{\alpha}_L^-$, $\delta\mathbf{U}_I$ and $\delta\boldsymbol{\alpha}_R^+$, the substitution of Eqs. (6) and (8) into Eq. (3) yields after rearrangements the following linear global system:

$$\begin{aligned} &\begin{bmatrix} \mathbf{B}_L^{-T} & \mathbf{0} & \mathbf{0} \\ \mathbf{0} & \mathbf{I} & \mathbf{0} \\ \mathbf{0} & \mathbf{0} & \mathbf{B}_R^{+T} \end{bmatrix} \left(\left(\begin{bmatrix} \mathbf{D}_{LL} & \mathbf{D}_{LI} & \mathbf{D}_{LR} \\ \mathbf{D}_{IL} & \mathbf{D}_{II} & \mathbf{D}_{IR} \\ \mathbf{D}_{RL} & \mathbf{D}_{RI} & \mathbf{D}_{RR} \end{bmatrix} \begin{bmatrix} \mathbf{B}_L^{-} & \mathbf{0} & \mathbf{0} \\ \mathbf{0} & \mathbf{I} & \mathbf{0} \\ \mathbf{0} & \mathbf{0} & \mathbf{B}_R^{+} \end{bmatrix} \right. \right. \\ &\qquad \left. \left. - \begin{bmatrix} \mathbf{T}_L^{-} & \mathbf{0} & \mathbf{0} \\ \mathbf{0} & \mathbf{0} & \mathbf{0} \\ \mathbf{0} & \mathbf{0} & \mathbf{T}_R^{+} \end{bmatrix} \right) \begin{Bmatrix} \boldsymbol{\alpha}_L^- \\ \mathbf{U}_I \\ \boldsymbol{\alpha}_R^+ \end{Bmatrix} \\ &= - \begin{bmatrix} \mathbf{B}_L^{-T} & \mathbf{0} & \mathbf{0} \\ \mathbf{0} & \mathbf{I} & \mathbf{0} \\ \mathbf{0} & \mathbf{0} & \mathbf{B}_R^{+T} \end{bmatrix} \left(\left(\begin{bmatrix} \mathbf{D}_{LL} & \mathbf{D}_{LI} & \mathbf{D}_{LR} \\ \mathbf{D}_{IL} & \mathbf{D}_{II} & \mathbf{D}_{IR} \\ \mathbf{D}_{RL} & \mathbf{D}_{RI} & \mathbf{D}_{RR} \end{bmatrix} \begin{bmatrix} \mathbf{B}_L^{+} \\ \mathbf{0} \\ \mathbf{0} \end{bmatrix} \right. \right. \\ &\qquad \left. \left. - \begin{bmatrix} \mathbf{T}_L^{+} \\ \mathbf{0} \\ \mathbf{0} \end{bmatrix} \right) \boldsymbol{\alpha}_L^+. \end{aligned} \tag{9}$$

The unknown vectors $\boldsymbol{\alpha}_L^-$, $\mathbf{U}_I$ and $\boldsymbol{\alpha}_R^+$ are found by solving the above linear system at each frequency. If only the left semi-infinite waveguide is present, the system given by Eq. (9) is modified by removing the third row and column from matrices and the third element from vectors. The right cross-section surface, in this case, is traction free.

Modal bases of displacements and forces are needed. In this paper, they are obtained by using a SAFE technique, which is explained in the next subsection.

2.4. Semi-analytical finite element formulation

The SAFE method is used in order to determine the elastic guided modes for the left and right cross-sections of the interior region. This technique reduces the analysis of three dimensional waveguides to two dimensions by using a spatial Fourier transform along the propagation direction ($\mathbf{u}(x,y,z) = \mathbf{u}(x,y)e^{+jkz}$, where k is the wavenumber and z is the propagation direction). Therefore, only the cross-sections have to be meshed, which allows a fast and accurate computation of eigenmodes (wavenumbers and modeshapes) for any arbitrary cross-section.

The SAFE variational formulation can be written as:

$$\delta\mathbf{U}\left(\mathbf{K}_1 - \omega^2\mathbf{M}_S - jk\left(\mathbf{K}_2 - \mathbf{K}_2^T\right) + k^2\mathbf{K}_3\right)\mathbf{U} = 0\ , \tag{10}$$

obtained from the following elementary matrices:

$$\begin{aligned} \mathbf{K}_1^e &= \textstyle\int_{S^e} \mathbf{B}_1^T\mathbf{C}\mathbf{B}_1\ dS\ , \quad \mathbf{K}_3^e = \int_{S^e} \mathbf{B}_2^T\mathbf{C}\mathbf{B}_2\ dS\ , \\ \mathbf{K}_2^e &= \textstyle\int_{S^e} \mathbf{B}_2^T\mathbf{C}\mathbf{B}_1\ dS\ , \quad \mathbf{M}_S^e = \int_{S^e} \rho\mathbf{N}^{eT}\mathbf{N}^e\ dS\ , \end{aligned}$$

where $\mathbf{B}_1 = \mathbf{L}_x\mathbf{N}^e_{,x} + \mathbf{L}_y\mathbf{N}^e_{,y}$ and $\mathbf{B}_2 = \mathbf{L}_z\mathbf{N}^e$ ($\mathbf{N}^e_{,x}$ and $\mathbf{N}^e_{,y}$ are the differentiation of the interpolation functions with respect to x and y, respectively). In the above equation, when the left (right) section is considered, $\mathbf{U}$ and S

would designate $\mathbf{U}_L$ ($\mathbf{U}_R$) and S_L (S_R). $\mathbf{L}_x$, $\mathbf{L}_y$ and $\mathbf{L}_z$ are defined as follows:

$$\mathbf{L}_x = \begin{bmatrix} 1 & 0 & 0 \\ 0 & 0 & 0 \\ 0 & 0 & 0 \\ 0 & 1 & 0 \\ 0 & 0 & 1 \\ 0 & 0 & 0 \end{bmatrix}, \mathbf{L}_y = \begin{bmatrix} 0 & 0 & 0 \\ 0 & 1 & 0 \\ 0 & 0 & 0 \\ 1 & 0 & 0 \\ 0 & 0 & 0 \\ 0 & 0 & 1 \end{bmatrix}, \mathbf{L}_z = \begin{bmatrix} 0 & 0 & 0 \\ 0 & 0 & 0 \\ 0 & 0 & 1 \\ 0 & 0 & 0 \\ 1 & 0 & 0 \\ 0 & 1 & 0 \end{bmatrix}. \tag{11}$$

For more details, the reader can refer to Hayashi et al. (2003) for instance.

By fixing the angular frequency ω and finding the wavenumber k, Eq. (10) leads to a quadratic eigenvalue problem. This eigenproblem can be linearized (see e.g. Tisseur and Meerbergen (2001)). The resolution of this system for the left (right) cross-section gives wavenumbers k_{Ln} (k_{Rn}) and modeshapes $\mathbf{U}_{Ln}$ ($\mathbf{U}_{Rn}$). The separation into ingoing and outgoing modes then yields the displacement modal bases $\mathbf{B}^{\pm}_{L,R}$ used in the previous subsection.

The next step is to determine the modal bases of forces $\mathbf{T}^{\pm}_{L,R}$. The idea is to derive forces directly from SAFE matrices. For clarity, let us first consider the right cross-section. From the third left integral of Eq. (1) and the application of normal mode expansions, forces on the right section can be rewritten as:

$$\delta\mathbf{U}_R^T\,\mathbf{f}_R = \int_{S_R} \delta\mathbf{u}^T \left(\sum_{n=1}^{N_R^+} \alpha^+_{Rn}\mathbf{t}^+_{Rn}\right) dS. \tag{12}$$

For one element e of surface S_R^e, $\delta\mathbf{u}^T = \delta\mathbf{U}^{e^T}\mathbf{N}^{e^T}$. Besides, following the same approach as in Treyssède (2008) for computing the energy velocity, it can be verified that $\mathbf{t}^+_{Rn} = \mathbf{L}_z^T\boldsymbol{\sigma}^+_{Rn} = \mathbf{L}_z^T\mathbf{C}\left(\mathbf{B}_1 + jk^+_{Rn}\mathbf{B}_2\right)\mathbf{U}^{+e}_{Rn}$. The substitution of

this expression into Eq. (12) yields:

$$\delta \mathbf{U}_R^T \, \mathbf{f}_R = \delta \mathbf{U}_R^T \sum_{n=1}^{N_R^+} \alpha_{Rn}^+ \left(\mathbf{K}_2 + j k_{Rn}^+ \mathbf{K}_3 \right) \mathbf{U}_{Rn}^+. \tag{13}$$

The above result defines explicitly the forces $\mathbf{f}_{Rn}^+$, involved inside the modal basis $\mathbf{T}_R^+$ of the previous subsection, as:

$$\mathbf{f}_{Rn}^+ = \left(\mathbf{K}_2 + j k_{Rn}^+ \mathbf{K}_3 \right) \mathbf{U}_{Rn}^+. \tag{14}$$

where $\mathbf{K}_2$ and $\mathbf{K}_3$ are the SAFE matrices associated with the right section. Following the same approach for the left section, the same kind of expression is obtained for the left forces $\mathbf{f}_{Ln}^\pm$:

$$\mathbf{f}_{Ln}^\pm = \left(\mathbf{K}_2 + j k_{Ln}^\pm \mathbf{K}_3 \right) \mathbf{U}_{Ln}^\pm, \tag{15}$$

where $\mathbf{K}_2$ and $\mathbf{K}_3$ are the SAFE matrices now associated with the left section.

Once the displacement modal bases are obtained, the calculation of modal bases $\mathbf{T}_L^\pm$ and $\mathbf{T}_R^+$ is then direct from Eqs. (14) and (15) and consistent with the used FE approximation. For hybrid FE-SAFE methods, this may simplify greatly the tedious post-process of consistent loads based on displacement derivatives associated with each mode.

2.5. Power coefficients

The definition of the power flow through a surface S ($S = S_L$ or S_R) is given by:

$$P = \int_S \bar{\mathbf{P}} \cdot \mathbf{n} \, dS, \tag{16}$$

where $P_i = -\sigma_{ij} \dot{u}_j$ is the Poynting vector and the bar denotes time averaging. This yields:

$$P = -j \frac{\omega}{4} \int_S (\mathbf{u}^{*T} \mathbf{t} - \mathbf{u}^T \mathbf{t}^*) dS. \tag{17}$$

The power of one single mode n, denoted P_{nn}, can then be directly obtained from:

$$P_{nn} = |\alpha_n|^2 \frac{\omega}{2} \Im \left(\mathbf{U}_n^{*T} \mathbf{f}_n \right), \tag{18}$$

$\Im$ designates the imaginary part.

For conciseness of notations, the subscripts L and R are omitted as well as superscripts $\pm$. However, one should be careful with such a definition when checking energy conservation in computations involving flexural modes. Auld's orthogonality relationship (Auld, 1973) states that:

$$(k_m - k_n^*) P_{mn} = 0, \tag{19}$$

with:

$$P_{mn} = -j \frac{\omega}{4} \int_S (\mathbf{u}_m^{*T} \mathbf{t}_n - \mathbf{u}_n^T \mathbf{t}_m^*) dS. \tag{20}$$

Eq. (19) shows that mode orthogonality $P_{mn} = 0$ holds for $k_m \neq k_n^*$. Double roots $k_m = k_n^*$ typically occur for flexural modes in cylinders. Thus, the power of a superposition of two flexural modes m and n might not be equal to the sum of their individual powers (Gunawan and Hirose, 2004). In such a case, the power flow P'_{mn} of such modes ought to be calculated as follows:

$$P'_{mn} = \frac{\omega}{2} \Im \left(\left\{ \begin{array}{c} \alpha_m \\ \alpha_n \end{array} \right\}^{*T} \left[\begin{array}{cc} \mathbf{U}_m & \mathbf{U}_n \end{array} \right]^{*T} \left[\begin{array}{cc} \mathbf{f}_m & \mathbf{f}_n \end{array} \right] \left\{ \begin{array}{c} \alpha_m \\ \alpha_n \end{array} \right\} \right). \tag{21}$$

Hence, P'_{mn} represents the total power associated with the couple of modes (m,n).

Finally, the power reflection and transmission coefficients are computed by dividing the reflected and transmitted powers by the incident power, re-

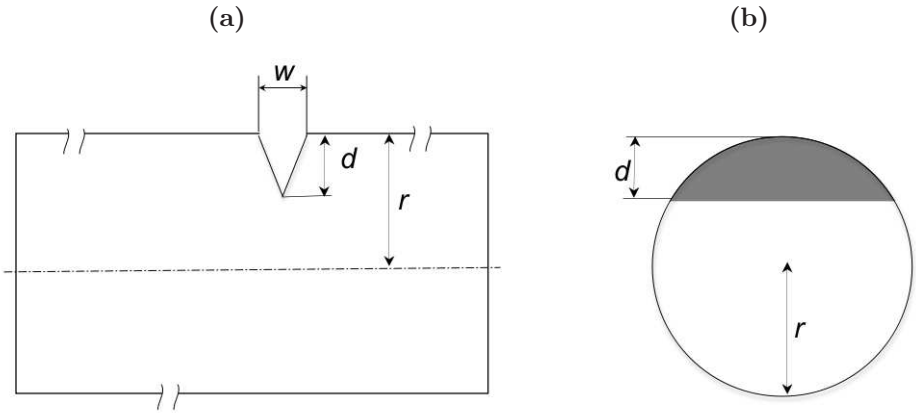

Figure 2: Description of a vertical non-axisymmetric crack: side view (a) and cross-section view (b).

spectively:

$$R_{mn} = \frac{P^-_{Ln}}{P^+_{Lm}},\ T_{mn} = \frac{P^+_{Rn}}{P^+_{Lm}}\ , \tag{22}$$

where m is the incident mode, n is the reflected or transmitted mode, and P^+_{Lm}, P^-_{Ln} and P^+_{Rn} are computed with Eq. (18) (or Eq. (21) for flexural modes).

3. Numerical results for vertical discontinuities

This section gives a detailed study of the interaction of fundamental guided modes (L(0,1), T(0,1) and F(1,1)) with vertical discontinuities.

3.1. Generalities

In the following, a steel circular cylinder with radius r is considered in simulations. The values of the Poisson coefficient, the density and the Young modulus are: $\nu = 0.25$, $\rho = 7800\ kg/m^3$ and $E = 2 \times 10^{11}\ Pa$, respectively.

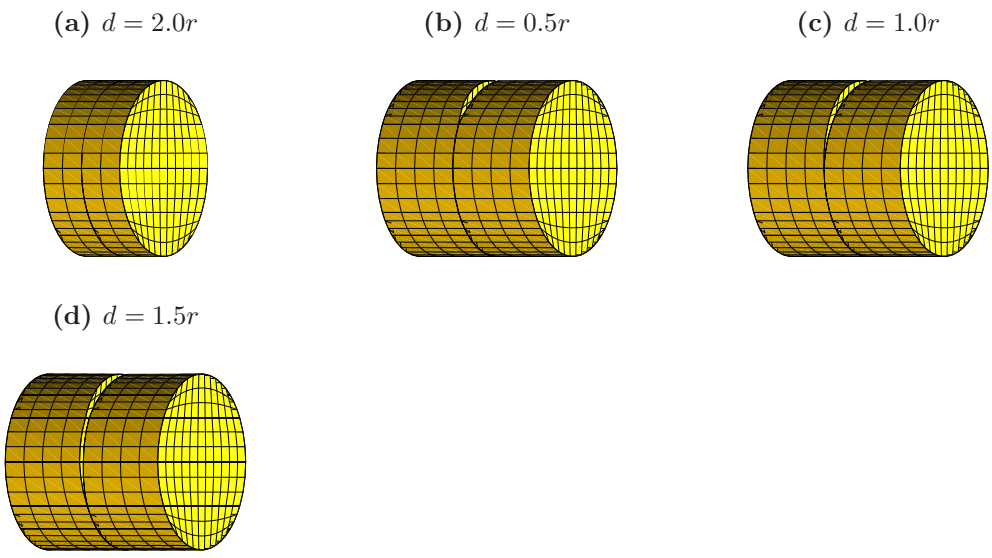

Figure 3: Meshing of a cylinder with a free-end of $d = 2.0r$ (a) and vertical cracks of depths of $0.5r$ (b), $1.0r$ (c) and $1.5r$ (d).

The dimensionless frequency is $\Omega = \omega \frac{r}{c_L}$ where c_L is the longitudinal velocity. The crack geometry considered in this section is depicted in Fig. 2. It can be referred to as a transverse notch (Mohr and Höller, 1976) characterised by an arbitrary maximum depth d and an area located in the vertical transverse plane at a given z.

Figure 3a depicts the FE mesh used for a free-end cylinder equivalent to a vertical crack of depth $d = 2.0r$ which leads to 4128 dofs. Figs. 3b-d represent the meshing of an infinite cylinder with a depth-variant vertical crack. The opening widths (w) of cracks is small with respect to the wavelength considered so that its effect can be neglected. The only crack parameter is hence the ratio $\frac{d}{r}$. The selected incident mode is launched at the left section of the cylinder with a unit amplitude. Structures are meshed with quadratic

hexahedrons with 20 nodes per element. The maximum element length is $h = 0.2r$ yielding $\frac{min(\lambda)}{h} > 10$, where $\lambda = \frac{2\pi r}{\Omega}$. The rough criterion of $h < \frac{\lambda}{4}$ for quadratic elements is hence quite satisfied.

It should be emphasized that the modal expansions used at the left and right sections also account for non-propagating modes. This allows to set both sections relatively close to the crack thus reducing the FE system. In SAFE computations, the searching interval for the eigenmodes is $\Im(kr) \in [-5; +5]$, $\forall\Omega$. These computed modes are all retained in the modal expansions of the hybrid method. A good accuracy is expected because the amplitudes of non-propagating modes scattered from cracks, but not retained in the expansions, would then be divided by at least $e^5 \simeq 148$ at cross-section boundaries, which are located at $z = \mp r$ (see Fig. 3). This has been further confirmed by numerical tests (not shown here) performed by changing the number of modes in the truncation.

Figure 4 shows the dispersion curves of dimensionless energy velocity versus dimensionless frequency obtained with the SAFE method on one of the two identical sections. Mode labels are in accordance with Meitzler (1961).

3.2. Free-end cylinder: numerical validation

This section deals with the scattering of the L(0,1) and F(1,1) modes from the free-end cylinder. The frequency ranges of both modes are chosen to enable the comparison with results found in the literature (Gregory and Gladwell, 1989; Rattanawangcharoen et al., 1994; Taweel et al., 2000). Modal expansions are applied to the left section while the right section and the surrounding surface are traction free.

Figure 5 depicts the power reflection coefficients when the L(0,1) mode

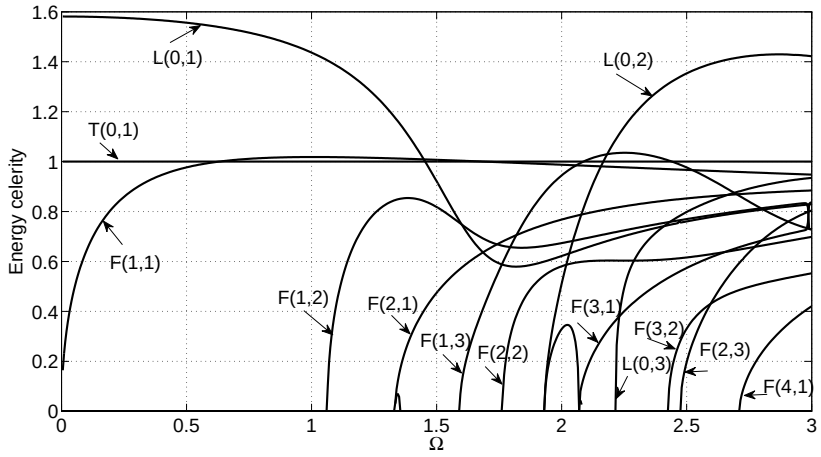

Figure 4: Dispersion curves of dimensionless energy velocity versus dimensionless frequency

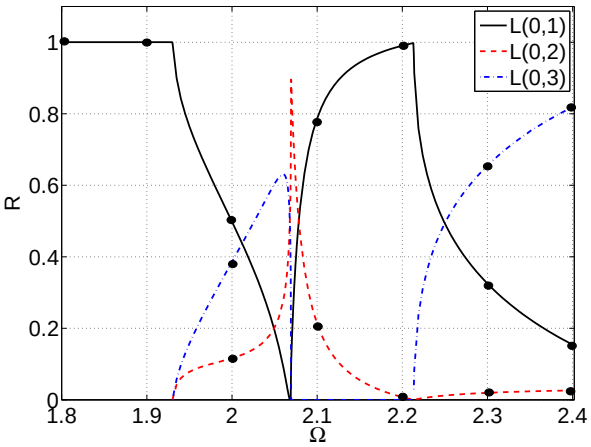

Figure 5: Power reflection coefficients of compressional modes L(0,1) (—), L(0,2) (−−) and L(0,3) (− ·) when the L(0,1) mode encounters a free-end cylinder. The bullets (•) are results found in Gregory and Gladwell (1989).

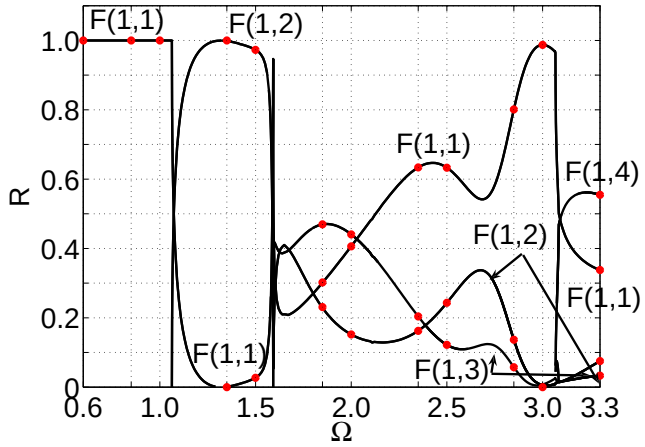

Figure 6: Power reflection coefficients of flexural modes when the F(1,1) mode encounters a free-end cylinder. The bullets (•) are results found in Taweel et al. (2000).

encounters a free-end cylinder. The range of the dimensionless frequency Ω is restricted to vary between 1.8 and 2.4. As expected, no mode conversions to flexural modes are observed due to the axisymmetric geometry. These results are compared with those obtained by Gregory and Gladwell (1989). A very good agreement is found.

Figure 6 shows the power reflection coefficients when the F(1,1) mode interacts with a free-end cylinder. The range of the dimensionless frequency Ω, in this case, varies between 0.6 and 3.3. As before, no mode conversions to compressional modes are observed. These results compare successfully with those obtained by Taweel et al. (2000).

The obtained results validate the modal expansion procedure at cross-section boundaries and its implementation.

3.3. Infinite cylinder: non-axisymmetric crack analysis

In this section, the scattering by non-axisymmetric damages is analysed for vertical cracks having three different depths and for the incident L(0,1), F(1,1) and T(0,1) modes. Modal expansions are now applied on both the left and right sections. The surfaces of cracks and the surrounding surface are traction free.

First, a numerical test has been performed on the cylinder without cracks ($d = 0$). Though not presented for conciseness, results have shown that incident modes on one side are fully transmitted to the other side with negligible reflection.

It is emphasised that singularities at crack corners are not taken into account in the FE models. However, as already found by Bai et al. (2001) and Alleyne et al. (1998), it is expected that inaccuracy remains only very close to the singularities without affecting the global behaviour in the far field and hereby, the power reflection and transmission coefficients. In this paper, it has been also checked that refining the mesh near the crack corner does not affect the computation of reflection and transmission coefficients.

3.3.1. Compressional mode L(0,1)

Figures 7a and 7b illustrate the power reflection (R) and transmission (T) coefficients of the compressional L(0,1) mode when it encounters a crack with the following depths: $d = 0.5r$, $1.0r$ and $1.5r$. As can be seen from Fig. 7a, R is significant except for the case of the crack with $d = 0.5r$. Fig. 7b shows that T is more sensitive to all depths including $d = 0.5r$. Note that the sharp changes of both coefficients coincide with the cut-off frequencies of different compressional and flexural modes (see Fig. 4). Moreover, as opposed

(a) L(0,1)

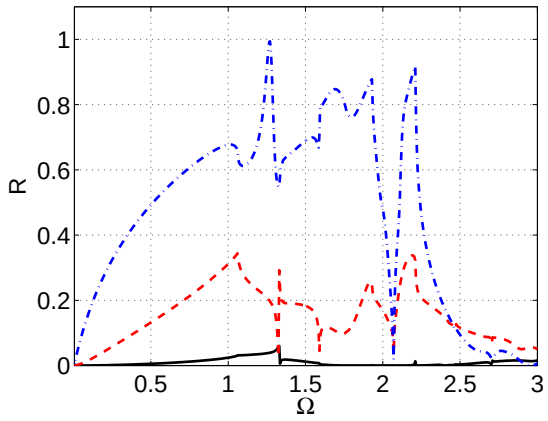

(b) L(0,1)

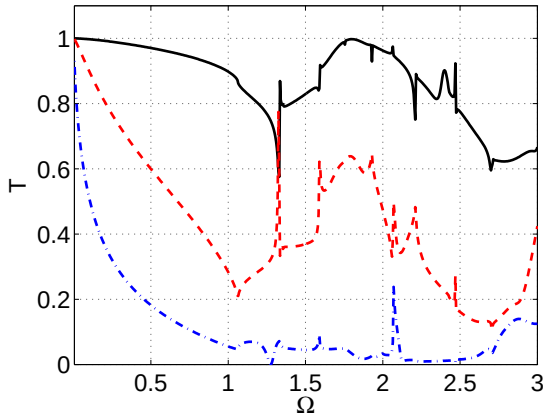

Figure 7: Power reflection (a) and transmission (b) coefficients of the compressional mode L(0,1) when the L(0,1) mode encounters a crack with depths $d = 0.5r$ (—), $d = 1.0r$ (−−) and $d = 1.5r$ (− ·).

to the free-end case, the axisymmetric L(0,1) mode is converted to flexural modes due to the non-axisymmetric nature of vertical cracks. These mode conversions are discussed in the following.

As shown in Fig. 4, the L(0,1) mode is less dispersive below the first cut-off frequency of the F(1,2) mode ($\Omega_c = 1.06$). R and T reveal a monotonic variation with the crack depth over the range defined by the first cut-off frequency (Figs. 7a and b). According to this and due to the fact that the single L(0,1) mode can be easily launched in this frequency range, this fundamental compressional mode is expected to be a good candidate for experiments.

Figures 8a and 8b depict the power reflection coefficients of the converted L(0,3) and F(1,1) modes from the incident L(0,1) mode. The L(0,3) mode presents a significant mode conversion above its cut-off frequency except for $d = 0.5r$. In the very low frequency range ($\Omega < 0.2$), it can be observed that the sensitivity of the converted F(1,1) mode is of the same order of magnitude as the reflected L(0,1) mode (Fig. 8b). R and T of the converted mode L(0,2) and T of L(0,3) are found to be insignificant in value and are not shown for conciseness. R and T of the converted flexural modes lower than 0.12 for the whole frequency range are not shown either. As in the free-end cylinder case, note that no mode conversion to the torsional T(0,1) mode has been found. This might be explained by the specificity of the T(0,1) mode, which is non-dispersive and whose displacement field remains in the cross-section plane.

For these computations, it has been verified that the sum of the power reflection and transmission coefficients at each frequency equals unity with a

(a) L(0,3)

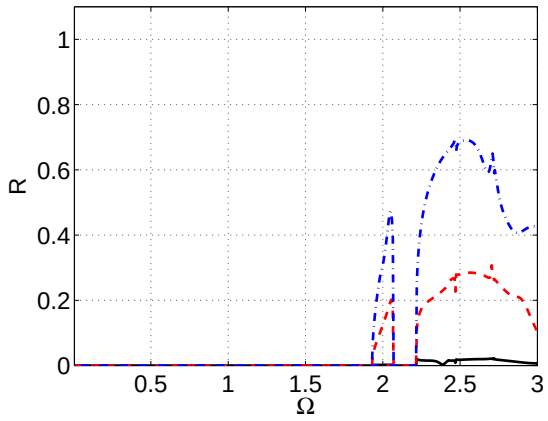

(b) F(1,1)

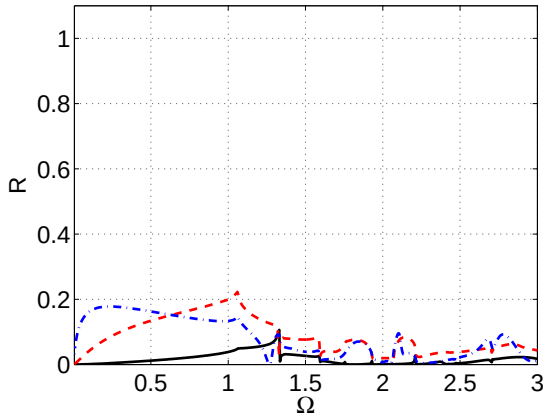

Figure 8: Power reflection coefficient of the L(0,3) (a) and F(1,1) (b) modes when the L(0,1) mode encounters a crack with depths $d = 0.5r$ (—), $d = 1.0r$ (−−) and $d = 1.5r$ (− ·).

maximum error of 0.2%.

3.3.2. Torsional mode T(0,1)

Figures 9a and 9b show the power reflection and transmission coefficients of the torsional mode T(0,1) when it encounters the vertical cracks.

In the low-frequency range, the T(0,1) mode exhibits a monotonic increase in the amplitude of the power reflection coefficient (and a decrease in the amplitude of the power transmission coefficient) with increasing crack depth. However, this behaviour is limited to a shorter frequency range in the case of the T(0,1) mode, up to approximately $\Omega = 0.2$ against $\Omega = 1$ for the L(0,1) Mode. From Ω=0.2 to 1.0, the reflected T(0,1) mode appears to be less attractive than the L(0,1) mode because of the non-monotonic variation of its amplitude with crack depth. Under the cut-off frequency of the F(1,2) mode, we note that the sensitivity of the T(0,1) mode is very low for a crack depth $d = 0.5r$, as observed earlier for the L(0,1) mode case.

In the frequency range $1 < \Omega < 3$, the reflected T(0,1) mode turns out to be more sensitive to a crack of depth $0.5r$ than the reflection of the L(0,1) mode (compare Figs. 7a and 9a). As for the incident L(0,1) mode, T is globally more sensitive than R. Although strong local changes may occur at cut-off frequencies, a monotonic increase of R with crack depth is found at certain frequencies in $[2.0, 3.0]$.

According to the non dispersive nature of the T(0,1) mode and since this is the only torsional mode to propagate in this frequency range, this confers to the fundamental T(0,1) mode potential interest for long-range non-destructive testing of low vertical crack depths.

Figure 10 depicts R of the converted flexural mode F(1,1) when T(0,1)

(a) T(0,1)

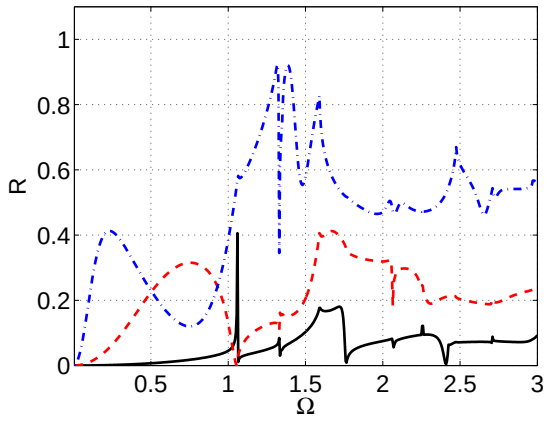

(b) T(0,1)

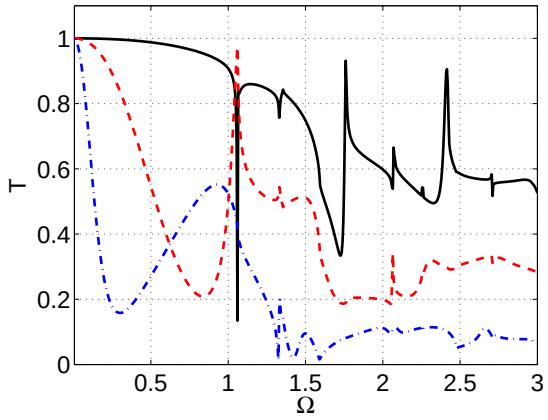

Figure 9: Power reflection (a) and transmission (b) coefficients of the torsional mode T(0,1) when it encounters a crack with depths $d = 0.5r$ (—), $d = 1.0r$ (−−) and $d = 1.5r$ (− ·).

(a) F(1,1)

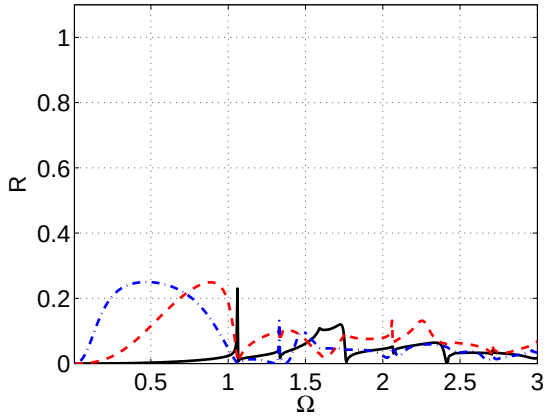

Figure 10: Power reflection coefficient of the flexural mode F(1,1) when the T(0,1) mode encounters a crack with depths $d = 0.5r$ (—), $d = 1.0r$ (−−) and $d = 1.5r$ (− ·).

encounters the cracks. As can be observed, R remains small except below the cut-off frequency of the F(1,2) mode. T, being of the same order of magnitude as R, is omitted for brevity and so are the converted flexural modes having insignificant values. No mode conversion to the compressional modes L(0,1), L(0,2) or L(0,3) has been found in this frequency range. For these computations, the maximum error on the power balance is 0.07%.

3.3.3. Flexural mode F(1,1):

The flexural mode F(1,1) corresponds to double eigensolutions having the same wavenumber but modeshapes of different orientations. Analytically, one mode is in $cos(\theta)$, the other is in $sin(\theta)$ (θ being the azimuthal coordinate in the cylindrical system). Consequently, the scattering of both F(1,1) modes will be different when non-axisymmetric cracks are considered. This can be

(a) F(1,1)

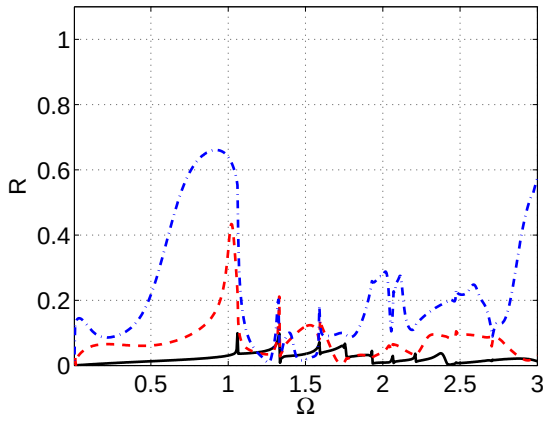

(b) F(1,1)

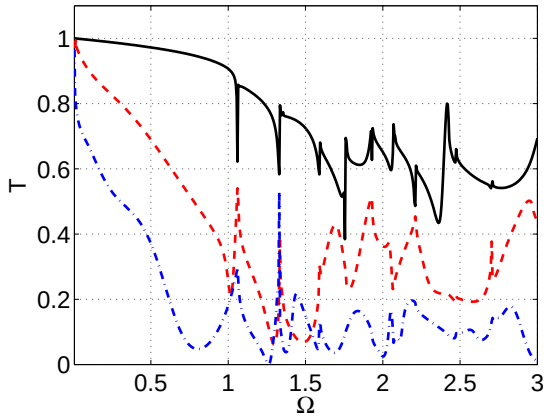

Figure 11: Power reflection (a) and transmission (b) coefficients of the flexural mode F(1,1) when the F(1,1) mode encounters a crack with depths $d = 0.5r$ (—), $d = 1.0r$ (−−) and $d = 1.5r$ (− ·).

(a) F(1,2)

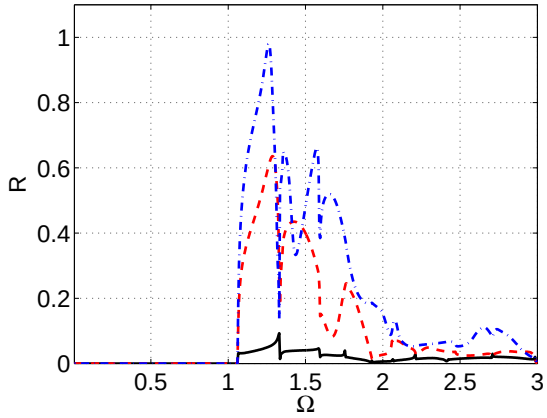

Figure 12: Power reflection coefficient of the flexural mode F(1,2) when the F(1,1) mode encounters a crack with depths $d = 0.5r$ (—), $d = 1.0r$ (−−) and $d = 1.5r$ (− ·).

overcome by launching "rotating" F(1,1) modes, written in terms of $e^{\pm i\theta}$ (instead of $cos(\theta)$ or $sin(\theta)$): at a given axial position z, the displacement field of such modes is indeed time-rotating in the cross-section so that the whole section is "scanned". Hence, the incident mode F(1,1) in $e^{\pm i\theta}$ will be scattered identically by non-axisymmetric vertical cracks. In the following results, the SAFE method gives modes in $cos(\theta)$ and $sin(\theta)$ but the incident mode F(1,1) is chosen as a linear combination $cos(\theta) + isin(\theta) = e^{i\theta}$, yielding a rotating mode.

Figures 11a and 11b show R and T of the flexural mode F(1,1) when it encounters the cracks. Their abrupt changes coincide with cut-off frequencies as for the modes mentioned earlier. R is not very sensitive to cracks except for the case $d = 1.5r$ at some frequencies. In addition, similar to the incident L(0,1) and T(0,1) modes, T is more sensitive than R.

R of the converted flexural mode F(1,2) is depicted in Fig. 12. It is worth noting the strong reflection of the incident F(1,1) mode into the F(1,2) flexural one near Ω=1.25. Due to the low dispersion of both flexural modes around this frequency (the F(1,2) mode is located near a maximum of energy velocity) and the slower velocity of the F(1,2) mode, flexural polarized waves in this frequency region could provide valuable information to experimental crack detection.

Though results are not shown here, significant mode conversions to the reflected F(2,2) mode and to the transmitted F(2,1) are also found. The reflected mode F(1,3) is only sensitive to the case of $d = 1.5r$. The other converted flexural modes are not sensitive to these crack depths (less than 0.06).

For these computations, the maximum error on the power balance is less than 0.13%.

4. Application to oblique free-ends and cracks

In order to highlight the potential of the hybrid 3D FE-SAFE method, this section is devoted to the study of the fundamental L(0,1) mode interaction with oblique discontinuities. The sensitivity of this mode to different inclination angles is illustrated.

Figure 13a sketches an oblique free-end cylinder of angle ϕ with respect to the vertical plane. The inclined crack is shown in Fig. 13b. The range of the dimensionless frequency Ω is chosen to vary between 0 and 3 as in the previous subsections (see e.g. Sec.3.3.1). The material characteristics and

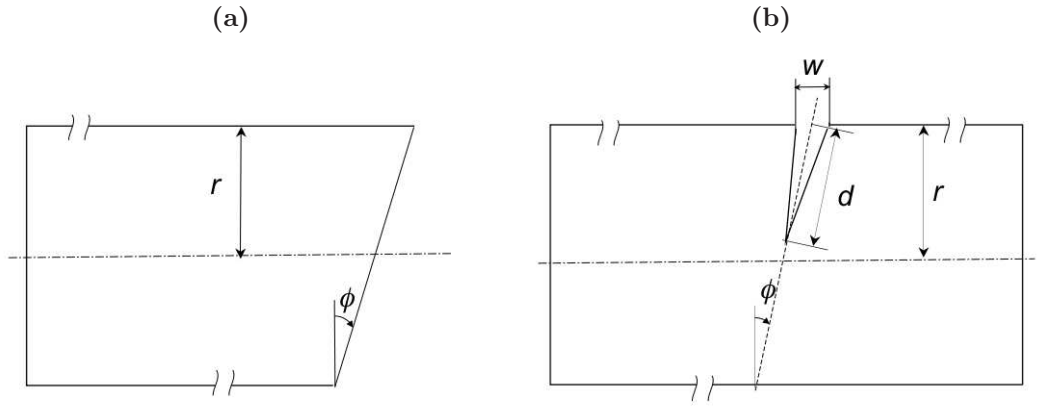

Figure 13: Description of an oblique free-end cylinder (a) and an oblique crack (b).

cylinder radius are the same as those in Sec. 3.1.

Figure 14 shows the power reflection coefficients (R) when the L(0,1) mode encounters free-ends with an inclination angle ϕ of 0°, 10° and 20°. As observed in this figure, R is sensitive to the free-end inclination. For oblique free-ends, R starts to decrease before the cut-off frequency of L(0,2) and L(0,3) modes, which does not occur for the vertical free-end cylinder ($\phi = 0°$). This is explained by mode conversions to flexural modes due to the non-axisymmetry of oblique free-ends. In this figure, it is observed that R decreases as ϕ increases in the frequency range $\Omega < 1.9$.

The maximum error on the power balance computations is less than 0.38%.

Figures 15a and b depict the power reflection (R) and transmission (T) coefficients when the L(0,1) mode encounters cracks of depth $d = 1.0r$. One

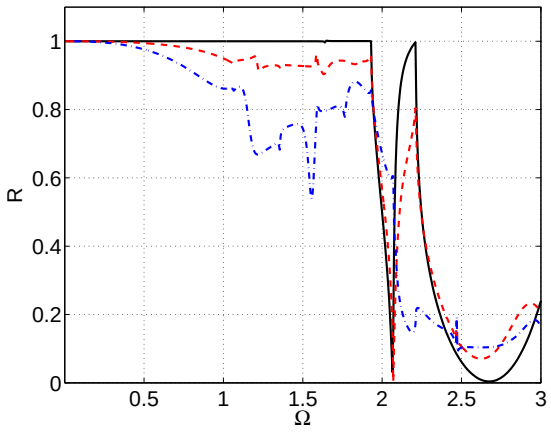

Figure 14: Power reflection coefficients of the compressional mode L(0,1) when it encounters a free-end cylinder of angle 0° (—), 10° (−−) and 20° (− ·).

vertical crack ($\phi = 0°$) and two oblique cracks ($\phi = 10°$ and $20°$) are studied. It can be observed that the maximum difference is located around frequencies $\Omega = 1.0$ and 2.7. In the low frequency range ($\Omega < 0.8$), L(0,1) has a low sensitivity to crack inclination.

Figure 16 represents the power reflection coefficients (R) of the converted F(1,1) mode from the incident L(0,1) mode. A significant mode conversion to the F(1,1) mode is observed for the three inclination angles. The reflection coefficients are very close to each other for $\phi = 10°$ and $20°$. However, it can be noticed that a stronger mode conversion occurs for $\phi = 10°$ and $20°$ around the frequency $\Omega = 1.0$.

A maximum error of 0.14% on the power balance is found for these computations.

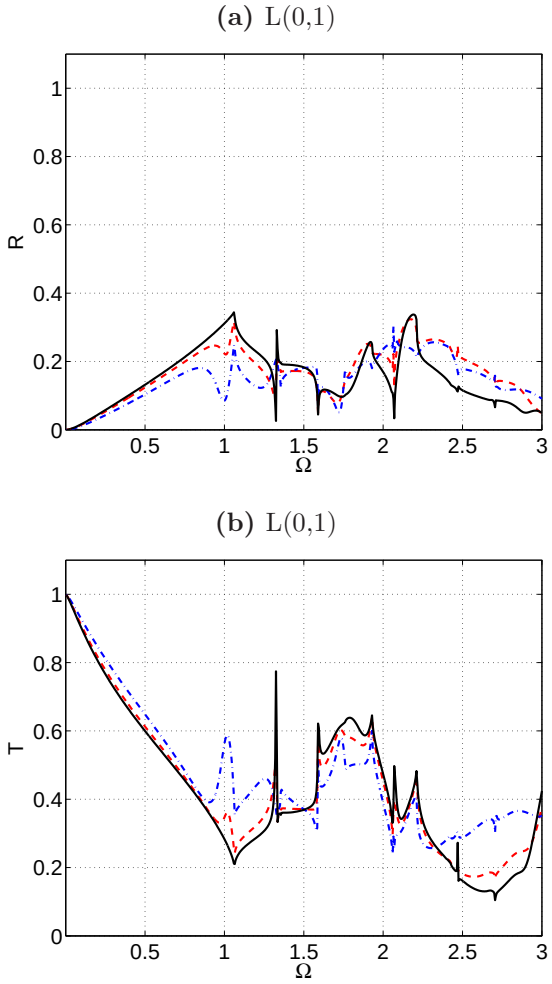

Figure 15: Power reflection (a) and transmission (b) coefficients of the compressional mode L(0,1) when it encounters a $d = 1.0r$ crack depth of angle 0° (—), 10° (−−) and 20° (− ·).

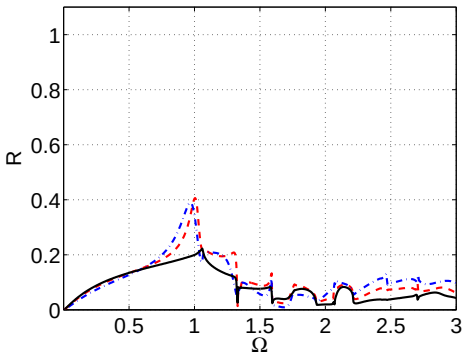

Figure 16: Power reflection coefficients of the flexural mode F(1,1) when the L(0,1) mode encounters a $d = 1.0r$ crack depth of angle 0° (—), 10° (−−) and 20° (− ·).

From a NDT point of view, it could be concluded that a good sensitivity of the L(0,1) mode to the considered inclination angles is observed when it interacts with free-ends (full cracks). However, this sensitivity is poor for oblique cracks whose depth is lower than the cylinder radius except at particular frequencies.

5. Conclusions

In this paper, a 3D hybrid numerical method has been developed for the investigation of wave scattering in elastic waveguides. This method combines the classical FE method and the so-called SAFE technique. It has the main advantage of being able to handle complex-shape inhomogeneities and waveguides of arbitrary cross-sections. Moreover, it gives a formula that renders straightforward the calculation of eigenforces and modal power flows. The validation of the hybrid 3D method has been established for the case of a free-end cylinder by comparing results with those of the literature. Then,

the analysis of the scattering of the fundamental longitudinal, torsional and flexural modes in circular cylinders with non-axisymmetric vertical cracks of different depths has been carried out. Cylinders with oblique free-ends and oblique cracks with different inclination angles have also been considered. The interactions of the L(0,1) mode with these discontinuities have been briefly studied. As pointed out throughout the analysis, the proposed method is likely to provide valuable information to further improve experimental investigation on cracks detection and characterisation. It has to be emphasised that the method is quite versatile and that complex-shaped damages can be readily handled.

Acknowledgements

This research work is part of the project ACTENA (Auscultation des Câbles Tendus Non Accessibles) funded by the French ANR (Agence National de Recherche) and EDF (Électricité De France) and piloted by LCPC (Laboratoire Central des Ponts et Chaussées).

References

Al-Nassar, Y., Datta, S., Shah, A., March 1991. Scattering of lamb waves by a normal rectangular strip weldment. Ultrasonics 29, 125–132.

Alleyne, D., Cawley, P., 1992. The interaction of lamb waves with defects. IEEE Trans. Ultras. Ferroelectr. Freq. control 39 (3), 381–397.

Alleyne, D. N., Lowe, M. J. S., Cawley, P., 1998. The reflection of guided waves from circumferential notches in pipes. Journal of Applied Mechanics 65 (3), 635–641.

Auld, B., 1973. Acoustic fields and waves in solids. Vol. II. A Wiley-Interscience publication.

Bai, H., Shah, A. H., Popplewell, N., Datta, S. K., 2001. Scattering of guided waves by circumferential cracks in steel pipes. ASME Journal of Applied Mechanics 68 (4), 619–631.

Baronian, V., Bonnet-Ben-Dhia, A. S., Lunéville, E., 2010. Transparent boundary conditions for the harmonic diffraction problem in an elastic waveguide. Journal of Computational and Applied Mathematics 234 (6), 1945–1952.

Benmeddour, F., Grondel, S., Assaad, J., Moulin, E., 2008a. Study of the fundamental lamb modes interaction with asymmetrical discontinuities. NDT & E International 41 (5), 330–340.

Benmeddour, F., Grondel, S., Assaad, J., Moulin, E., 2008b. Study of the fundamental lamb modes interaction with symmetrical notches. NDT & E International 41 (1), 1–9.

Castaings, M., Le Clézio, E., Hosten, B., 2002. Modal decomposition method for modeling the interaction of Lamb waves with cracks. J. Acoust. Soc. America 112 (6), 2567–2582.

Damljanović, V., Weaver, R. L., 2004. Propagating and evanescent elastic waves in cylindrical waveguides of arbitrary cross section. J. Acoust. Soc. Am. 115 (4), 1572–1581.

Datta, S., Shah, A., Karunasena, W., 1999. Ultrasonic waves and material

and defect characterization in composite plates. Mechanics of Composite Materials and Structures 6, 285–300.

Demma, A., Cawley, P., Lowe, M., 2003. Scattering of the fundamental shear horizontal mode from steps and notches in plates. J. Acoust. Soc. Am. 113 (4), 1880–1891.

Demma, A., Cawley, P., Lowe, M., Roosenbrand, A., Pavlakovic, B., 2004. The reflection of guided waves from notches in pipes: a guide for interpreting corrosion measurements. NDT & E Int. 37, 167–180.

Ditri, J., 1994. Utilization of guided elastic waves for the characterization of circumferential cracks in hollow cylinders. J. Acoust. Soc. Am. 96 (6), 3769–3775.

Galán, J., Abascal, R., 2003. Elastodynamic guided wave scattering in infinite plates. Int. J. Numer. Meth. Engng 58, 1091–1118.

Galán, J., Abascal, R., 2005. Lamb mode conversion at edges. a hybrid boundary element-finite-element solution. J. Acoust. Soc. America 117 (4), 1777–1784.

Gavrić, L., 1995. Computation of propagative waves in free rail using a finite element technique. Journal of Sound and Vibration 185 (3), 531–543.

Gregory, R., Gladwell, I., 1989. Axisymmetric waves in a semi-infinite elastic rod. Q. JI Mech. appl. Math. 42 (2), 327–337.

Gunawan, A., Hirose, S., 2004. Mode-exciting method for lamb wave-scattering analysis. J. Acoust. Soc. Am. 115 (3), 996–1005.

Hayashi, T., Song, W.-J., Rose, J., 2003. Guided wave dispersion curves for a bar with an arbitrary cross-section, a rod and rail example. Ultrasonics 41, 175–183.

Hayashi, T., Tamayama, C., Murase, M., 2006. Wave structure analysis of guided waves in a bar with arbitrary cross-section. Ultrasonics 44, 17–24.

Hladky-Hennion, A., 1996. Finite element analysis of the propagation of acoustic waves in waveguides. Journal of Sound and Vibration 194 (2), 119–136.

Hladky-Hennion, A., Langlet, P., Billy, M., 1997. Finite element analysis of the propagation of acoustic waves along waveguides immersed in water. Journal of Sound and Vibration 200 (4), 519–530.

Karunasena, W., Liew, K., Kitipornchai, S., 1995. Hybrid analysis of lamb wave reflection by a crack at the fixed edge of a composite plate. Computer methods in applied mechanics and engineering 125, 221–233.

Karunasena, W., Shah, A., Datta, S., 1991. Plane-straine-wave scattering by cracks in laminated composite plates. Journal of Engineering Mechanics 117 (8), 1738–1754.

Karunasena, W., Shah, A., Datta, S., 1994. Guided waves in a jointed composite plate. J. Acoust. Soc. Am. 95 (3), 1208–1212.

Lagasse, P., 1973. Higher-order finite-element analysis of topographic guides supporting elastic surface waves. J. Acoust. Soc. Am. 53 (4), 1116–1122.

Le Clézio, E., Castaings, M., Hosten, B., 2002. The interaction of the S0 Lamb mode with vertical cracks in an aluminum plate. Ultrasonics 40, 187–192.

Lowe, M., Alleyne, D., Cawley, P., 1998. Defect detection in pipes using guided waves. Ultrasonics 36, 147–154.

Lowe, M., Diligent, O., 2002. Low-frequency reflection characteristics of the s0 lamb wave from a rectangular notch in a plate. J. Acoust. Soc. America 111 (1), 64–74.

Ma, J., Simonetti, F., Lowe, M., 2006. Scattering of the fundamental torsional mode by an axisymmetric layer inside a pipe. J. Acoust. Soc. Am. 120 (4), 1871–1880.

Mal, A., Chang, Z., 2000. A semi-numerical method for elastic wave scattering calculations. Geophys. J. Int. 143, 328–334.

Meitzler, A. H., 1961. Mode coupling occurring in the propagation of elastic pulses in wires. The Journal of the Acoustical Society of America 33 (4), 435–445.

Mohr, W., Höller, P., 1976. On inspection of thin-walled tubes for transverse and longitudinal flaws by guided ultrasonic waves. IEEE Transactions on Sonics and Ultrasonics 23 (5), 369 – 373.

Moreau, L., Castaings, M., Hosten, B., Predoi, M., 2006. An orthogonality relation-based technique for post-processing finite element predictions of waves scattering in solid waveguides. J. Acoust. Soc. Am. 120 (2), 611–620.

Predoi, M., Castaings, M., Moreau, L., 2008. Influence of material viscoelasticity on the scattering of guided waves by defects. J. Acoust. Soc. Am. 124 (5), 2883–2894.

Rattanawangcharoen, N., Shah, A. H., Datta, S. K., 1994. Reflection of waves at the free edge of a laminated circular cylinder. Journal of Applied Mechanics 61 (2), 323–329.

Rattanawangchroen, N., Zhuang, W., Shah, A., Datta, S., October 1997. Axisymmetric guided waves in jointed laminated cylinders. Journal of Engineering Mechanics, 1020–1026.

Shkerdin, G., Glorieux, C., 2004. Lamb mode conversion in a plate with a delamination. J. Acoust. Soc. America 116 (4), 2089–2100.

Shkerdin, G., Glorieux, C., 2005. Lamb mode conversion in an absorptive bi-layer with a delamination. J. Acoust. Soc. Am. 118 (4), 2253–2264.

Taweel, H., Dong, S., Kazic, M., 2000. Wave reflection from the free end of a cylinder with an arbitrary cross-section. Internation Journal of Solids and Structures 37, 1701–1726.

Tisseur, F., Meerbergen, K., 2001. The quadratic eigenvalue problem. SIAM REVIEW 43 (2), 235 – 286.

Treyssède, F., 2008. Elastic waves in helical waveguides. Wave Motion 45, 457–470.

Zhao, Z., Rose, J. L., 2003. Boundary element mode for defect characteriza-

tion potential in a wave guide. International Journal of Solids and Structures 40, 2645 – 2658.

Zhou, W., Ichchou, M., Mencik, J., 2009. Analysis of wave propagation in cylindrical pipes with local inhomogeneities. Journal of Sound and Vibration 319, 335–354.

Zhuang, W., Shah, A. H., Datta, S. K., 1997. Axisymmetric guided wave scattering by cracks in welded steel pipes. ASME Journal of Pressure Vessel Technology 119 (4), 401–406.